Type: PhD summary
Section: Image Processing and Imaging Techniques
Participant in the 5th Ed. Justiniano Casas Prize (2016)

Retinal Image Analysis: Image Processing and Feature Extraction Oriented to the Clinical Task

Análisis de imagen retiniana: Procesado de imagen y extracción de características orientado a la tarea clínica

Andrés G. Marrugo[1*], María S. Millán[2S].

[1]. *Facultad de Ingeniería, Universidad Tecnológica de Bolivar, Km 1 vía Turbaco, Cartagena, Colombia*

[2]. *Dep. Òptica i Optometria, Universitat Politècnica de Catalunya BARCELONATECH, C/Violinista Vellsolà, 37, 08222 Terrassa (Barcelona), Spain*

(*) E-mail: agmarrugo@unitecnologica.edu.co S: SEDOPTICA member

DOI: 10.7149/OPA.50.1.49507

ABSTRACT:

Medical digital imaging has become a key element of modern health care procedures. It provides visual documentation and a permanent record for the patients, and most important the ability to extract quantitative information about many diseases. Modern ophthalmology relies on the advances in digital imaging and computing power. In this paper we present an overview of the results from the doctoral dissertation by Andrés G. Marrugo. This dissertation contributes to the digital analysis of retinal images and the problems that arise along the imaging pipeline of fundus photography, a field that is commonly referred to as *retinal image analysis*. We have dealt with and proposed solutions to problems that arise in retinal image acquisition and longitudinal monitoring of retinal disease evolution. Specifically, non-uniform illumination compensation, poor image quality, automated focusing, image segmentation, change detection, space-invariant (SI) and space-variant (SV) blind deconvolution (BD). Digital retinal image analysis can be effective and cost-efficient for disease management, computer-aided diagnosis, screening and telemedicine and applicable to a variety of disorders such as glaucoma, macular degeneration, and retinopathy.

Key words: Computer-aided diagnosis, medical image, retinal image, telemedicine, ophthalmology.

RESUMEN:

La captura de imagen digital es una parte fundamental de los procedimientos médicos modernos. Provee de documentación visual, un registro permanente para los pacientes y la posibilidad de extraer información cuantitativa sobre muchas enfermedades. La oftalmología depende considerablemente del análisis digital de imágenes. En este trabajo se presentan los resultados principales de la tesis doctoral de Andrés G. Marrugo. Este trabajo contribuye al análisis digital de tales imágenes y los problemas que surgen a lo largo del proceso de formación de imagen. Este campo se le conoce como *análisis de imagen retiniana*. En esta tesis se han propuesto soluciones a problemas asociados con la adquisición de imagen retiniana y la detección de cambios temporales en patologías retinianas. Específicamente, los problemas de iluminación no-uniforme, baja calidad de imagen, enfoque automático, y análisis multi-canal. Sin embargo, existen situaciones inevitables en que se adquieren imágenes de baja calidad, como imágenes emborronadas debido a las aberraciones del ojo. Este problema lo hemos abordado utilizando dos metodologías para la deconvolución ciega de imágenes. En la primera

aproximación, consideramos que el emborronamiento es invariante espacialmente y en la segunda aproximación extendimos el trabajo y propusimos un método más general espacialmente variante.

Palabras clave: diagnóstico asistido por computador, imagen médica, imagen retiniana, telemedicina, oftalmología.

REFERENCES AND LINKS / REFERENCIAS Y ENLACES

[1] M. D. Abramoff, M. Garvin, and M. Sonka, "Retinal Imaging and Image Analysis," Biomedical Engineering, IEEE Reviews **3**, 169–208, (2010). https://doi.org/10.1109/RBME.2010.2084567

[2] A. G. Marrugo, "Comprehensive Retinal Image Analysis: Image Processing and Feature Extraction Techniques Oriented to the Clinical Task.," Universitat Politècnica de Catalunya, Barcelona, (2013). http://hdl.handle.net/10803/134698

[3] A. G. Marrugo, M. S. Millan, G. Cristóbal, S. Gabarda, and H. C. Abril, "No-reference Quality Metrics for Eye Fundus Imaging," CAIP 2011, LNCS, **6854**, 486–493, (2011).

[4] S. Gabarda and G. Cristóbal, "Blind image quality assessment through anisotropy," J Opt Soc Am A Opt Image Sci Vis, **24** , B42–51, (2007). https://doi.org/10.1364/JOSAA.24.000B42

[5] Xiang Zhu and P. Milanfar, "Automatic Parameter Selection for Denoising Algorithms Using a No-Reference Measure of Image Content," IEEE Trans Image Process. **19**, 3116–3132, (2010). https://doi.org/10.1109/TIP.2010.2052820

[6] R. Ferzli and L. J. Karam, "A no-reference objective image sharpness metric based on the notion of just noticeable blur (JNB)," IEEE Trans Image Process. **18**, 717–728, (2009). https://doi.org/10.1109/TIP.2008.2011760

[7] Y. Qu, Z. Pu, H. Zhao, and Y. Zhao, "Comparison of different quality assessment functions in autoregulative illumination intensity algorithms," Opt. Eng. **45**, 117201, (2006). https://doi.org/10.1117/1.2388924

[8] A. G. Marrugo, M. S. Millan, G. Cristóbal, S. Gabarda, and H. C. Abril, "Anisotropy-based robust focus measure for non-mydriatic retinal imaging," J. Biomed. Opt., **17**, 076021, (2012). https://doi.org/10.1117/1.JBO.17.7.076021

[9] M. Moscaritolo, H. Jampel, F. Knezevich, and R. Zeimer, "An Image Based Auto-Focusing Algorithm for Digital Fundus Photography," IEEE Trans. Med. Imaging, **28**, 1703–1707, (2009). https://doi.org/10.1109/TMI.2009.2019755

[10] S. Nayar and Y. Nakagawa, "Shape from focus," IEEE Trans Pattern Anal Mach Intell, **16**, 824–831, (1994). https://doi.org/10.1109/34.308479

[11] K. Choi, J. Lee, and S. Ko, "New autofocusing technique using the frequency selective weighted median filter for video cameras," IEEE T. Consum. Electr., **45**, 820–827, (1999). https://doi.org/10.1109/30.793616

[12] M. Kristan, J. Pers, M. Perse, and S. Kovacic, "A Bayes-spectral-entropy-based measure of camera focus using a discrete cosine transform," Pattern Recognit. Lett., **27**, 1431–1439, (2006). https://doi.org/10.1016/j.patrec.2006.01.016

[13] A. G. Marrugo, M. S. Millan, and H. C. Abril, "Implementation of an image based focusing algorithm for non-mydriatic retinal imaging," Engineering Mechatronics and Automation (CIIMA), 2014 III International Congress of, 1–3, (2014). https://doi.org/10.1109/ciima.2014.6983425

[14] A. G. Marrugo, Ed., Anisotropy focus measure. [Online Accessed: 17-Apr-2016]. Available at: https://github.com/agmarrugo/anisotropy-focus/

[15] H. Narasimha-Iyer, A. Can, B. Roysam, C. Stewart, H. Tanenbaum, A. Majerovics, and H. Singh, "Robust detection and classification of longitudinal changes in color retinal fundus images for monitoring diabetic retinopathy," IEEE Trans. Biomed. Eng., **53**, 1084–1098, (2005) https://doi.org/10.1109/TBME.2005.863971

[16] A. G. Marrugo, F. Sroubek, M. Sorel, and M. S. Millan, "Multichannel blind deconvolution in eye fundus imaging," presented at the ISABEL '11-Proceedings of the 4th International Symposium on Applied

Sciences in Biomedical and Communication Technologies, **7**:1–5 (2011). https://doi.org/10.1145/2093698.2093705

[17] N. Everdell, I. Styles, A. Calcagni, J. Gibson, J. Hebden, and E. Claridge, "Multispectral imaging of the ocular fundus using light emitting diode illumination," Rev. Sci. Instrum., **81**, 093706–093709, (2010). https://doi.org/10.1063/1.3478001

[18] A. G. Marrugo, M. Sorel, F. Sroubek, and M. S. Millan, "Retinal image restoration by means of blind deconvolution," J. Biomed. Opt., **16**, 11, 116016, (2011). https://doi.org/10.1117/1.3652709

[19] C. Stewart, Chia-Ling Tsai, and B. Roysam, "The dual-bootstrap iterative closest point algorithm with application to retinal image registration," IEEE Trans. Med. Imaging, **22**, 1379–1394, (2003).

[20] T. Aach and A. Kaup, "Bayesian Algorithms for Change Detection in Image Sequences Using Markov Random Fields," Signal Process. Image **7**, 147–160, (1995) https://doi.org/10.1016/0923-5965(95)00003-F

[21] A. Levin, Y. Weiss, F. Durand, and W. Freeman, "Understanding Blind Deconvolution Algorithms," IEEE Trans Pattern Anal. Mach Intell., **12**, 2354–2367, (2011). https://doi.org/10.1109/34.990136

[22] A. G. Marrugo, M. S. Millan, G. Cristóbal, S. Gabarda, M. Sorel, and F. Sroubek, "Image analysis in modern ophthalmology: from acquisition to computer assisted diagnosis and telemedicine," presented at the Proceedings SPIE, **8436**, 84360C–84360C–10 (2012). https://doi.org/10.1117/12.921299

[23] C. Muramatsu, Y. Hayashi, A. Sawada, Y. Hatanaka, T. Hara, T. Yamamoto, and H. Fujita, "Detection of retinal nerve fiber layer defects on retinal fundus images for early diagnosis of glaucoma," J. Biomed. Opt., **15**, 016021, (2010). https://doi.org/10.1117/1.3322388

[24] L. Xu and S. Luo, "Optimal algorithm for automatic detection of microaneurysms based on receiver operating characteristic curve," J. Biomed. Opt., **15**, 065004, (2010). https://doi.org/10.1117/1.3523367

[25] P. Bedggood, M. Daaboul, R. Ashman, G. Smith, and A. Metha, "Characteristics of the human isoplanatic patch and implications for adaptive optics retinal imaging," J. Biomed. Opt., **13**, 024008, (2008). https://doi.org/10.1117/1.2907211

[26] A. G. Marrugo, M. S. Millan, M. Sorel, and F. Sroubek, "Restoration of retinal images with space-variant blur," J. Biomed. Opt., 19, no. 1, p. 016023, Jan. 2014. https://doi.org/10.1117/1.JBO.19.1.016023

[27] A. G. Marrugo, M. S. Millan, M. Sorel, J. Kotera, and F. Sroubek, "Improving the blind restoration of retinal images by means of point-spread-function estimation assessment," presented at the Tenth International Symposium on Medical Information Processing and Analysis, **9287**, 92871D (2015).

[28] M. Tallón, J. Mateos, S. D. Babacan, R. Molina, and A. K. Katsaggelos, "Space-variant blur deconvolution and denoising in the dual exposure problem," INFORMATION FUSION, (2012).

[29] A. G. Marrugo, M. S. Millan, M. Sorel, and F. Sroubek, "Blind restoration of retinal images degraded by space-variant blur with adaptive blur estimation," presented at the 8th Ibero American Optics Meeting/11th Latin American Meeting on Optics, Lasers, and Applications **8785,** 8785D1 (2013)

1. Introduction

When alluding to the eye, the posterior segment, or all regions behind the crystalline lens, we refer to it as the ocular fundus. The retina lies at the rear surface of the globe, and in ophthalmology, is an area of primary concern if visual loss is an issue not traceable to refractive error or problems in the cornea or the lens. Physicians have observed the eye fundus as early as 1850 with the invention of the ophthalmoscope by the German physician Hermann Von Helmholtz. Since then, many advances came forth both in quality and specific-purpose developments of techniques for imaging the eye fundus such as: fluorescent angiography, modern electronic fundus photography, stereo fundus photography, confocal laser ophthalmoscopy, among others [1].

To photograph the retina, it is usually required that the iris be dilated with pharmaceuticals and photographed with a *mydriatic* fundus camera (mydriatic means the iris must be dilated). A fundus camera (Fig. 1(a)) is a specialized low-power microscope with an attached camera designed to photograph the interior of the eye in association with the optical system of the eye. Retinal cameras can also be *non-mydriatic* in that the patient's natural dilation in a dark room is used. These cameras use near infrared light to focus and a white light arc lamp to produce a flash that illuminates the retina. The fundus images are captured using a conventional digital camera, attached to the retinal camera body designed to image the eye fundus in association with the optical system of the eye.

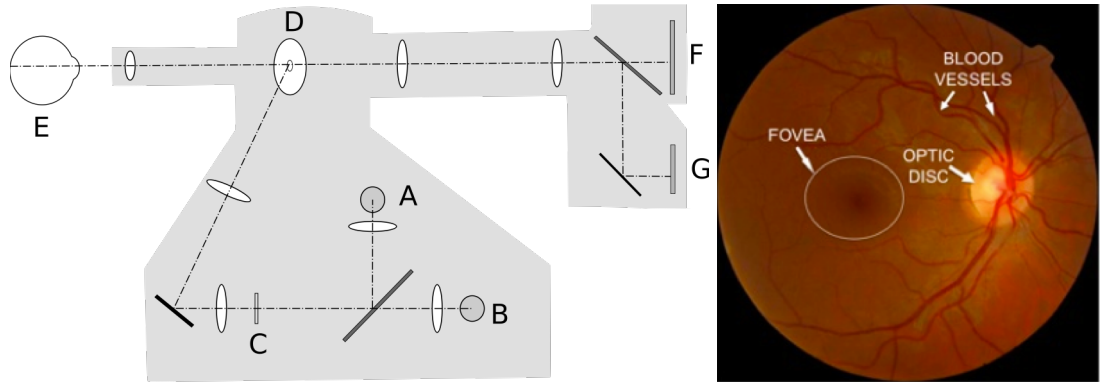

Fig. 1 (a) The optical pathway of the fundus camera. Light generated from either (A) the viewing lamp or (B) the electronic flash is projected through a (C) set of filters and lenses onto a mirror. This mirror reflects the light into a series of lenses that focus the light. The light is reflected by a (D) round mirror with a central aperture, exits the camera through the objective lens, and proceeds into the (E) eye through the cornea. The back-scattered light from the retina exits the cornea and continues through the central aperture of the previously described mirror, through the diopter compensation lenses, and then reaches the camera system: (F) the sensor and (G) the viewing screen. (b) A retinal Image.

A typical retinal image is shown in Fig. 1(b). The normal features include the optic disc, the fovea, and the blood vessels. The optic disc (or optic nerve head) is the location where ganglion cell axons exit the eye to form the optic nerve. The fovea is the part of the retina responsible for sharp central vision. It has the highest density of photoreceptor cells and approximately 50% of the nerve fibers in the optic nerve carry information from the fovea. The blood vessels or vasculature are the circulatory system that supplies blood to the different layers of the retina.

Many important diseases manifest themselves in the retina and find their origin in the eye, the brain, or the cardiovascular system. There are a number of prevalent diseases that can be studied via eye imaging and image analysis such as diabetic retinopathy (DR), age-related macular degeneration (AMD), glaucoma, and vascular diseases [1].

In this paper we present an overview of the results from the doctoral dissertation: “Comprehensive Retinal Image Analysis: Image Processing and Feature Extraction Techniques Oriented to the Clinical Task”[2]. We have dealt with and proposed solutions to problems that arise along the imaging pipeline of fundus imaging. The paper is organized as follows: in section 2 we describe our findings on image acquisition, image quality assessment and focusing metrics. In section 3, we discuss the results related to image change detection. In section 4, the different contributions for retinal image enhancement. And finally, in section 5 we draw conclusions.

2. Retinal Image Acquisition

2.a. Image Quality Assessment

Acquiring good quality retinal images is important in order to extract meaningful information that is medically relevant. Identifying good quality images is mainly a no-reference quality assessment problem in which there is no ground-truth.

In Ref. [3] we studied several no-reference quality metrics, namely (Q1) Image quality through anisotropy proposed by Gabarda & Cristóbal [4] which is based on measuring the variance of the expected entropy of a given image upon a set of predefined directions. (Q2) Local gradients and sharpness metric proposed in Ref. [5] that attempts to provide a quantitative measure of image sharpness whose value drops if the noise

variance increases or if the image content gets blurry. (Q3) The just noticeable blur proposed in Ref. [6] is a sharpness metric designed to be able to predict the relative amount of blurriness in images regardless of their content. It is an edge-based sharpness metric based on a human visual system model that makes use of probability summation over space. (Q4) The image variance, which has been shown to be monotonic has a straightforward relation with image quality [7]. In addition, we proposed a modification to (Q1) which included a weighting function over the field of view because fundus images are often not degraded uniformly throughout the image.

One of the experiments we carried out was to analyze a set of 20 fundus images divided in 5 subsets of 4 images corresponding to the same eye and acquired within the same session. All images within each subset have a varying degree of quality similar to the first subset shown in Fig. 2. The images were sorted in terms of image quality using the quality metrics (Q1-Q4) and by two optometrists recruited as readers A and B. The agreement between the reader and the quality metric was computed by a similarity score S that ranges from 0 to 1 implying no agreement or perfect agreement, respectively.

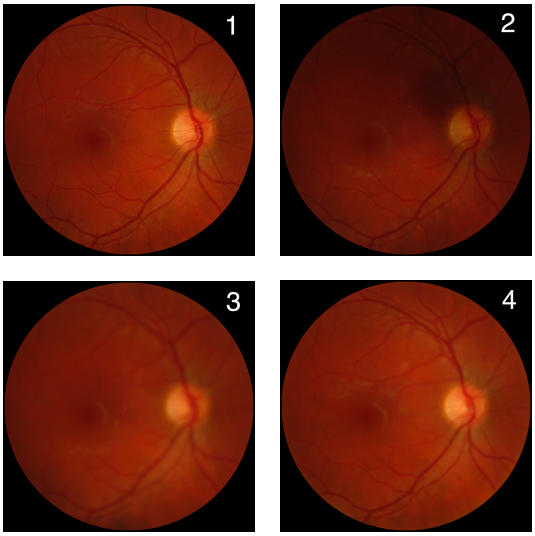

Fig. 2. Fundus images with varying degree of quality corresponding to the same eye.

The evaluation of the subset shown in Table and the whole set of images is shown in Table 1. From the considered metrics, Q1 is the most reliable in terms of agreement with expert assessment, evidenced by average similarity scores of 0.8 and 0.9 with readers A and B, respectively. Q1 performs a measure of anisotropy throughout the whole image. That is, quantifying the fact that structures change in a directional way is good indicator of image sharpness. What this means is that the visibility of retinal structures (caused either by poor illumination or blur) is one of the most important features to take into account when evaluating retinal image quality. The results lend strong support to the development of a no-reference metric for fundus imaging based on a type of anisotropy measure. This is exactly what we have done by further developing these findings into a focus measure for retinal imaging.

Table 1. Evaluation of the no-reference metrics (Q1-Q4) with respect to reader grading. The sub-index in S indicates reader A or B. The inter-reader agreement for the whole set of 20 images was 0.90

	Q1	Q2	Q3	Q4
S_A 1st subset	1.00	0.50	0.50	0.50
S_B 1st subset	1.00	0.50	0.50	0.50
S_A all images	0.80	0.55	0.55	0.40
S_B all images	0.90	0.60	0.65	0.45

2.b. Robust Automated Focusing

From the results obtained by evaluating image quality, we proposed a focus measure (FM) for non-mydriatic fundus imaging based on the anisotropic properties of image degradation [8]. The common FMs

are based on norm of gradient or second derivative of the image, gray level variance and energy of Laplacian. Surprisingly, little is known about the performance of these methods for fundus imaging and the literature on this subject is scarce.

In Ref. [8] we studied the performance of five notable approaches for comparison with our proposed method. The first FM (S1) was proposed in Ref. [9]. It is basically the variance of a low-pass filtering accompanied by median filtering. The second FM (S2) is the l2-norm of image gradient; the third FM (S3) is the energy of Laplacian. It can analyze high frequencies associated with image edges. The third FM (S4) is the summed modified Laplacian proposed by Nayar et al. [10] to overcome the drawbacks of FMs based on second order derivatives. The fifth FM (S5) is the Frequency-Selective Weighted Median (FSWM) Filter [11], a high-pass nonlinear filter based on the difference of medians.

The proposed focus measure (S*a*) is based on a weighted directional variance of the normalized discrete cosine transform (DCT) [12]. The normalization is carried out in order to achieve illumination invariance. The FM is optimized for near-infrared imaging because the fundus camera is non-mydriatic. A diagram that summarizes the algorithm is shown in Fig. 3. In order to reduce the computation time, the FM is applied to a small region of the image that contains retinal structures. This window is transformed to the DCT domain and a weighted directional sampling procedure is carried out. The weighting scheme was obtained from a training set of images, which yielded weights resembling a band-pass filter. The output is what we call a measure of anisotropy. The focus measure performance was compared, by means of simulated and real images, to S1-S5 focus measures.

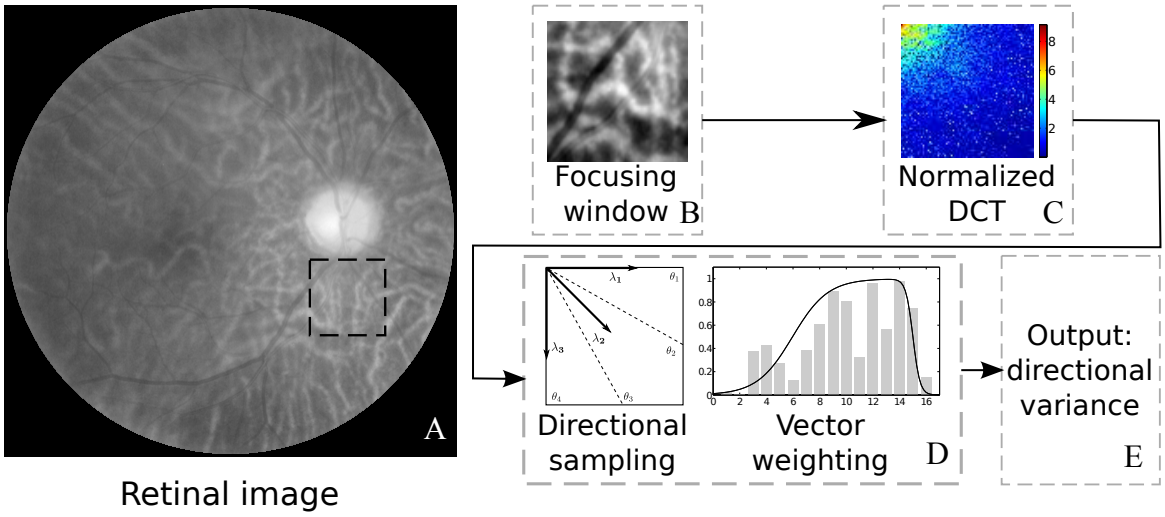

Fig. 3 Block diagram illustrating the focus measure algorithm.

The experimental set-up consisted mainly of an AF mechanism attached to a non-mydriatic digital fundus camera system (TRC-NW6S, Topcon, Tokyo Japan). The AF apparatus consisted of in-house assembled stepper motor mechanism for the displacement of the compensation lens controlled via RS232 with a PC. This mechanism was coupled to the fundus camera [13].

To test the robustness of the proposed FM, a set of 140 artificially degraded images were produced. The dataset consisted in blurring the images and then adding noise. We tested for Gaussian noise, Speckle noise, and Impulse noise. From these tests we concluded that S1, S4, and Sa performed the best. We then tested on real images. One of the experiments we carried out was to analyze the performance of the FMs in subjects of different ages. In Fig. 4 we show the focusing curves obtained from subjects with the ages: 27, 40, 68, and 70. In general, from the comparison against S1 and S4 it is clear that the proposed FM S*a* outperforms them in the considered cases. From the four cases shown only in one (Fig. 4(c)) the S*a* measure peak did not coincide precisely with the optimal focus position. However, the error is no more than a single position. The FMs curves of S1 and S4 are generally flatter than those of S*a* which in a focus search strategy is not wanted because of the difficulty to properly distinguish the optimum position in a coarse or initial search. In the other experiments the proposed measure outperformed the considered measures in robustness and accuracy. The code is available in [14].

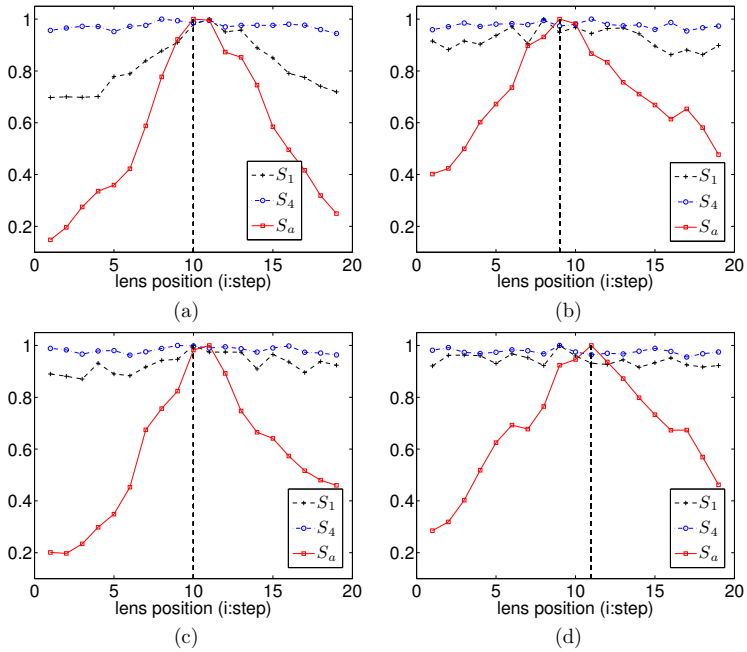

Fig. 4 Focusing curves obtained from four subjects with ages (a) 27, (b) 40, (c) 68, and (d) 70 years old. The dashed vertical line indicates the correct focused position.

3. Detection of Longitudinal Changes in Retinal Images

3.a. Illumination Compensation

Multiple image illumination compensation techniques are mainly motivated by the need for a processing strategy that requires two or more images, like in change detection [15], multichannel deconvolution [16], sequential multispectral imaging [17], etc. In Ref. [18] we described such a technique for compensating the uneven illumination distribution from two images of the same retina acquired at different moments for further processing. The basic idea is a follows: the illumination distribution can be compensated by adjusting the intensity values on one image to approximately match that of the other while satisfying a predetermined illumination model. Because the illumination of the retina is formed by a slowly varying light field over a smooth surface it can be modeled by a low-order parametric surface, in this case a 4th-order polynomial. The compensation is then formulated via a parametric surface fitting equation

$$\arg\min_{k} \left\| I_1(x,y) - k(x,y)\cdot I_2(x,y) \right\| , \qquad (1)$$

where I_1 and I_2 are the two retinal images, k is the illumination compensation function given by $k(x,y) = a_{15}y^4 + a_{14}y^3x + \ldots + a_2 + a_1$. Eq. (1) is minimized in the least squares sense to estimate the 15 parameters. In Fig. 5 we show an example of two retinal images and the compensation function $k(x,y)$. The different shades of gray indicate the average contrast and intensity difference between the two original images in Fig. 5 (a) and (b).

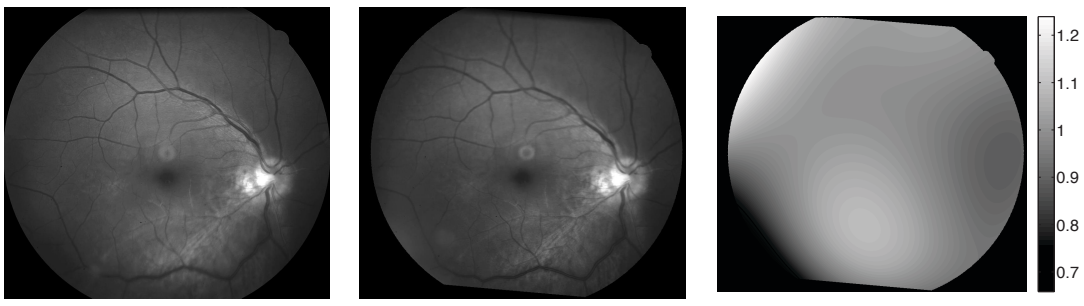

Fig. 5. Illumination compensation for two retinal images (a) and (b). (c) Compensation function *k*.

3.b. Detection of Longitudinal Changes

One of the main concerns of ophthalmologists when they visually compare fundus images of the same retina over time is to identify true structural or morphological changes pertaining to possible pathological damage. In the same inspection they must disregard other changes merely caused by variation of illumination or blur. A correct assessment of a patient's state evolution requires sharp images obtained on a regular time basis. However, this is not always guaranteed and is the main motivation for developing preprocessing techniques as the ones described in the previous section. Image registration is another preprocessing technique necessary for image-based longitudinal change assessment [19].

In this section we briefly describe a strategy for the identification of areas of structural change in time sequences of retinal images [18]. An initial step in order to identify these changes comes from computing the difference from the two registered images with previous illumination compensation,

$$\Delta I(x,y) = I_1(x,y) - I_2(x,y) \ . \tag{2}$$

An example of a difference image is shown in Fig. 6(c) in absolute value for visualization purposes. The structural changes can now be visualized and detected from the difference image $\Delta I(x,y)$ by taking a statistical significance test, as proposed in Ref. [15]. First, structural changes are often associated with a group of pixels, thus the change decision at a given pixel *j* should be based on a small block of pixels in the neighborhood of *j* denoted as w_j. Second, in the absence of any change, the difference can be assumed to be due to noise alone. Therefore, the decision as to whether or not a change has occurred corresponds to choosing one of two competing hypothesis: the *null hypothesis* $\mathcal{H}_0$ or the *alternative hypothesis* $\mathcal{H}_1$, corresponding to *no-change* and *change* decisions, respectively. Assuming a Gaussian distribution for the difference values, the changes can be identified by comparing the normalized sum square of the differences within the neighborhood w_j to a predetermined threshold τ as described by Aach et al. [20]. The test is carried out as below

$$\Omega_j = \frac{1}{\sigma_n^2} \sum_{(x,y)\in w_j} \Delta I(x,y)^2 \gtrless_{H_0}^{H_1} \tau \ , \tag{3}$$

where σ_n is the noise standard deviation of the difference in the no-change regions. The threshold τ is derived from the fact that Ω_j follows a χ^2 distribution with *N* degrees of freedom, where *N* is the number of pixels in the window w_j. It can be obtained for a particular false positive rate α from the χ^2 tables.

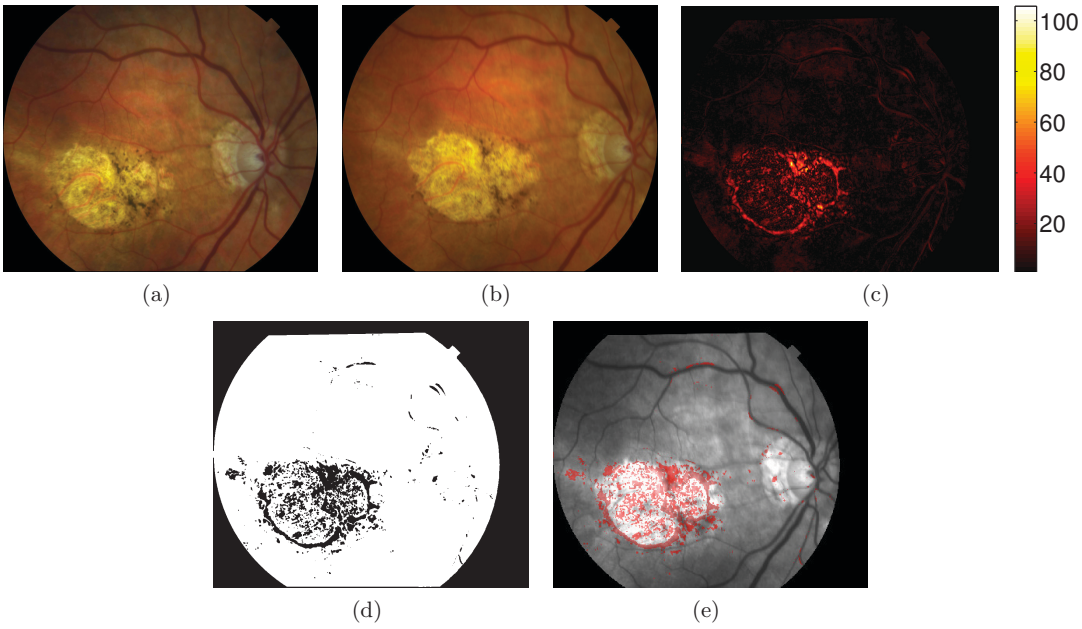

Fig. 6 Retinal image change detection: Images (a) I_1 and (b) I_2, (c) Image difference $\Delta I(x,y)$ in absolute value, (d) Image change map, and (d) Image change map in red on top of gray-scale retinal image.

The image change map resulting from the change detection test with an $\alpha = 0.05$ is shown in Fig. 6 (d). Notice that the central whitish region (pathological area) is the main cause of structural changes. To better understand this result, in Fig. 6(e) we show one of the retinal images in gray-scale where the pixels related to structural changes are highlighted in red. For further details the reader is referred to Ref. [18].

4. Retinal Image Restoration

In addition to uneven illumination fundus images often suffer from blurring. This hinders diagnosis and the evolution assessment of a disease. In this section we describe a method for fundus image deblurring by means of multichannel blind deconvolution. It consists of a series of preprocessing steps to adjust the images so they comply with the considered degradation model, followed by the estimation of the point spread function, and image deconvolution.

4.a. Space-Invariant (SI) Deconvolution

Blind deconvolution consists in the recovery of the original scene from a single or set of blurred images in the presence of a poorly determined or unknown point spread function (PSF) [21]. Here we consider multichannel blind deconvolution because it is better posed, as opposed to single-channel, and the PSF is estimated directly from the degraded images. The restoration strategy is given in Ref. [18]. As a regularization term it includes the total variation of the image, which provides good quality of restoration. To properly restore the images the degradation should be adequately modeled.

We assume two registered input images, I_1 and I_2, both originating from an ideal sharp image U

$$I_1 = U * h_1 + n_1$$
$$I_2 = (Uk^{-1}) * h_2 + n_2\,, \tag{4}$$

where $*$ is the standard convolution, h_i are called convolution kernels or PSFs and k is a function accounting for relative local illumination change between images. For pixels where no illumination changes occur $k \approx 1$. The noise n_i is assumed Gaussian additive with zero mean in both images. Despite the fact that we consider the PSFs to vary in time between the two image acquisitions, we assume them to be spatially invariant within each image.

The PSF estimation and image deconvolution algorithm can be viewed as a Bayesian maximum a posteriori estimation of the most probable sharp image and blur kernels. The algorithm is basically the minimization of the functional

$$\arg\min_{U,h_1,h_2} \tfrac{1}{2}\|U * h_1 - I_1\|^2 + \tfrac{1}{2}\|U * h_2 - kI_2\|^2 + \lambda_u \int |\nabla U| + \lambda_h \|I_1 * h_2 - kI_2 * h_1\|^2,$$
$$h_1, h_2 \geq 0\,, \tag{5}$$

with respect to the latent image U and blur kernels h_1 and h_2. The first and second terms measure the difference between the input blurred images and the searched image U blurred by kernels h_1 and h_2. The size of this difference is measured by L_2 norm $\|.\|$ and should be small for the correct solution. Ideally, it should correspond to the noise variance in the given image. Function k compensates for uneven illumination. The two remaining terms are regularization terms with positive weighting constants λ_u and λ_h. The third term is the total variation of U. It improves stability of the minimization and from the statistical viewpoint incorporates prior knowledge about the solution. The last term is a condition linking the PSFs of both images, which also improves the numerical stability of the minimization. For this procedure we set λ_u = 1000 and λ_h = 10. The functional is alternately minimized in the subspaces corresponding to the image and the PSFs. The minimization in the PSF subspace is equivalent to the solution of a system of linear equations in the least squares sense with the non-negativity constraint. In the same minimization procedure both the PSFs and the restored image are estimated. If I_1 and I_2 were acquired in a lapse of time, it would be necessary to introduce the structural change detection strategy (Section 0) in both the model of Eq. (4) and the functional given by Eq. (5) (Ref. [18]).

An example of a restored retinal image is shown in Fig. 7. In this example the PSF was estimated by Eq. (5), but we have performed deconvolution (restoration) with a single image and with both images to demonstrate the advantages of using multiple images in the restoration as well. From the profile of the original image not much detail can be properly resolved. In contrast there is a noticeable enhancement in both restored images in such a way that much more details are properly resolved. The multichannel

deconvolution overcomes the limitations of single-channel deconvolution due to information redundancy. The improvement in resolution is evidenced by gain in contrast and steeper slopes. Notice the small c-shaped blood vessel within the optic disc, and how they are much sharper and properly resolved in the multichannel restoration in Fig. 7 in comparison with the single-channel restoration and the original images. For a detailed examination of this topic see Refs. [16, 18, 22].

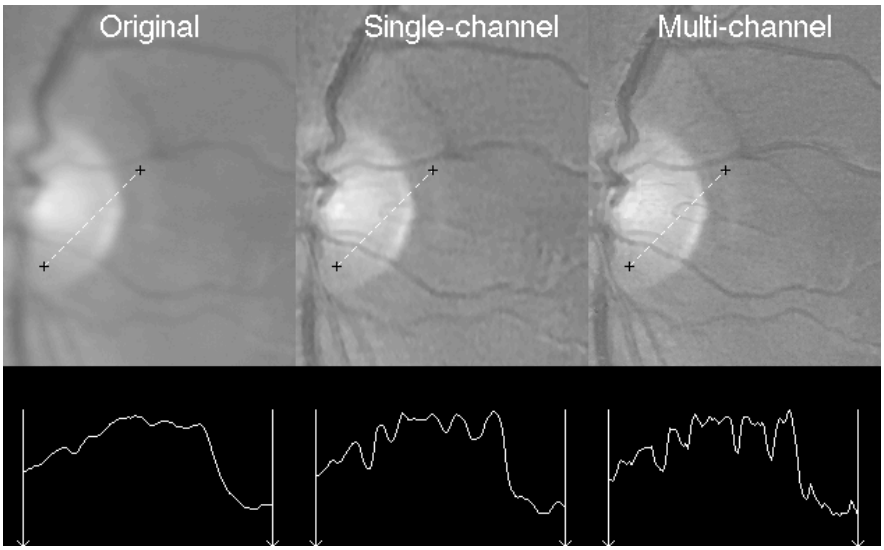

Fig. 7. (Top, from left to right) Detail from the original degraded retinal image, the restored version using single-channel deconvolution, and multi-channel deconvolution. (Bottom) Intensity profiles corresponding to the dashed segment. Note how the profiles depict the level of detail in each image.

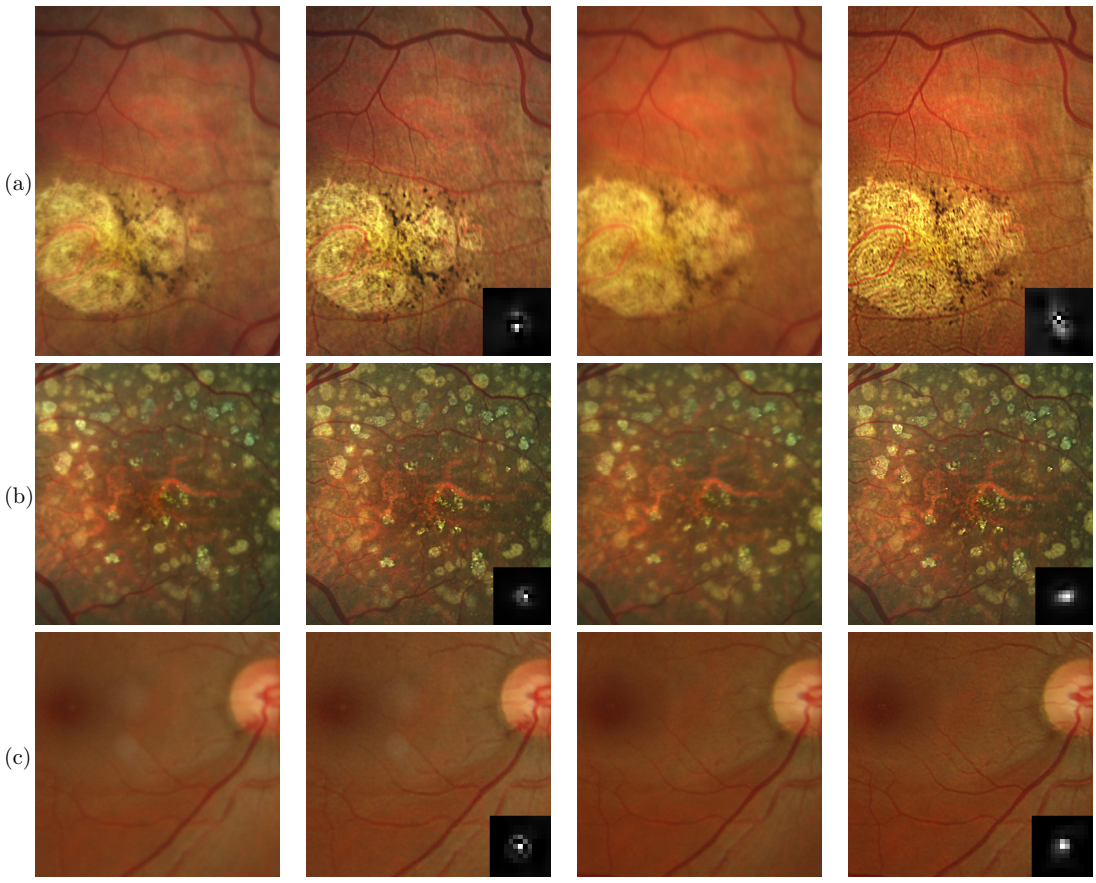

Fig. 8. Original and restored color retinal images; (a), (b) and (c) indicate three separate cases arranged from left to right degraded and restored images. The estimated PSF is shown at the bottom of the restored image.

We carried out several experiments to demonstrate the applicability of the proposed method for retinal image deblurring in real scenarios. Three different cases are shown in Fig. 8. The estimated PSFs are shown at the bottom of the restored images. All images contain some pathological damage and have been acquired within considerable lapses of time (several months). In all examples the resolution improvement can be visually assessed by the clear distinction of details such as small blood vessels or the increase in sharpness of edges particularly in the pathological areas. We emphasize the fact that these images correspond to real routine patient follow-up and were not intentionally degraded. From a clinical viewpoint, the enhancement can be used for a more precise assessment of a patient. Likewise, the images are more suitable for subsequent processing such as for the detection of retinal pathology [23, 24].

In Fig. 9 the same images are shown but in grey-scale to highlight the areas of structural change in pseudocolor. As we have mentioned earlier, this is an important result for its potential impact in the medical practice. Subtle changes can be identified by this approach such as the ones in Fig. 9(b) and the hemorrhage in the region of the optic disc in Fig. 9(c).

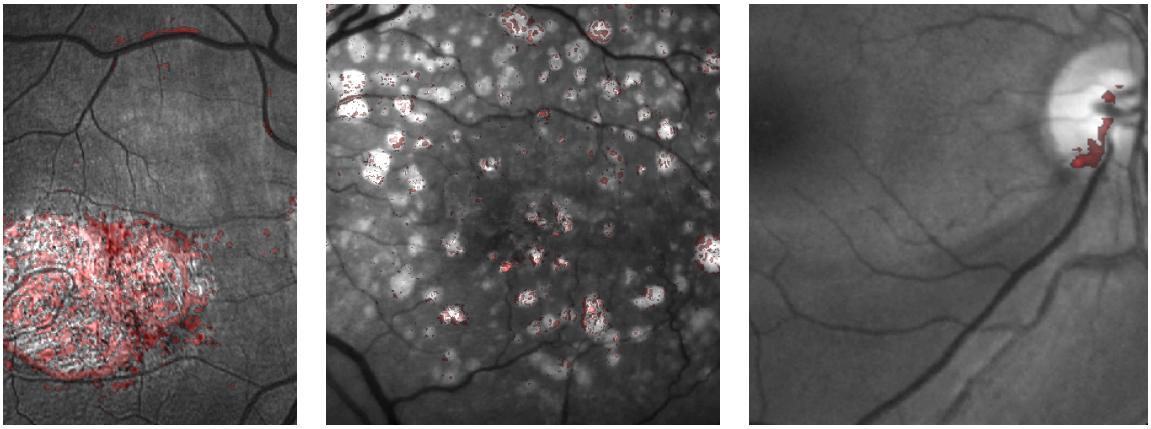

(a) (b) (c)

Fig. 9 Visualization of structural changes in pseudo-color for the images of Fig. 8.

4.b. Space-Variant (SV) Deconvolution

In the previous section we modeled the degradation as a space-invariant (SV) convolution. This approximation is valid as long as the PSF changes little throughout the field of view. In other words, that the blurring is homogenous. In reality we know that the PSF is indeed spatially variant [25], in such a way that in certain cases the space-invariant approach may fail. For that reason, we proposed a space-variant approach [26, 27]. To address this limitation we now model the blurred retinal image I by a general linear operator

$$I = Hu + n\,. \tag{6}$$

The operator H can be written in the following form

$$I(x,y) = [Hu](x,y) = \int u(s,t)h(s,t,x-s,y-t)\,dsdt\,, \tag{7}$$

where h the SV PSF. The operator H is a generalization of standard convolution where h is now a function of four variables. We can think of this operation as a convolution with a PSF $h(s,t,x,y)$ that is now dependent on the position (x,y) in the image.

An obvious problem of spatially varying blur is that the PSF is now a function of four variables. Except trivial cases, it is hard to express it by an explicit formula. Even if the PSF is known, we must solve the problem of a computationally efficient representation. In retinal imaging, all typical causes of blur change in a continuous gradual way, which is why we assume the blur to be locally constant. Therefore, we can make the approximation that locally the PSFs are space-invariant. By taking advantage of this property we do not have to estimate local PSFs for every pixel. Instead, we divide the image into rectangular windows and estimate only a small set of local PSFs (Fig. 10) following the method described in the previous section [18]. The estimated PSFs are assigned to the centers of the windows from where they were computed. In the rest of the image, the PSF h is approximated by bilinear interpolation from the four adjacent local PSFs (Fig. 11). The local PSF estimation procedure not always succeeds. The main reason why the kernel estimation fails

is due to the existence of textureless or nearly homogenous regions bereft of structures with edges (e.g. blood vessels) to provide sufficient information [28]. To identify them we devised an eye-domain knowledge strategy. The incorporation of proper a priori assumptions and domain knowledge about the blur into the method provides an effective mechanism for a successful identification of non-valid PSFs [27].

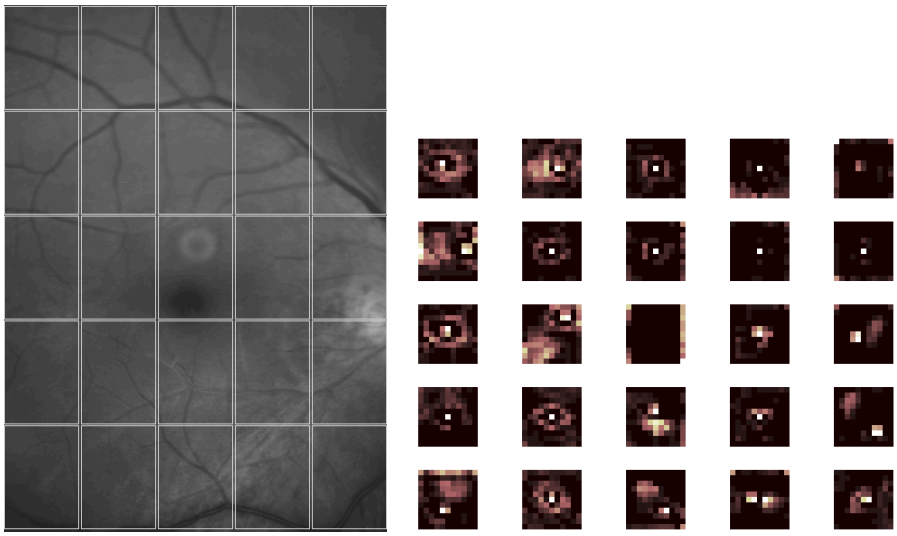

Fig. 10 Degraded retinal image with a 5 by 5 grid that defines the image patches. (b) Estimated local PSFs.

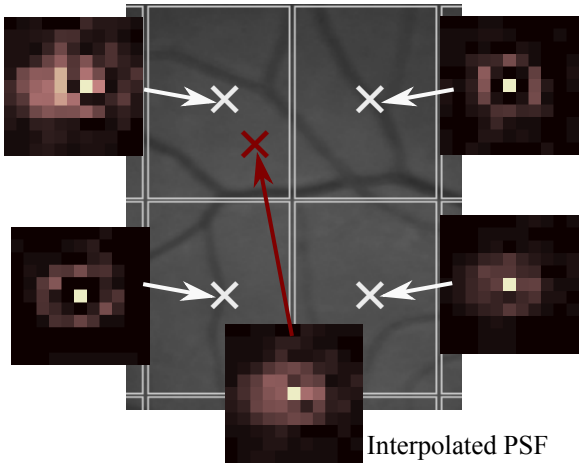

Fig. 11 Because the blur changes gradually, we can estimate convolution kernels on a grid of positions and approximate the PSF in the rest of the image (bottom kernel) by interpolation from four adjacent kernels.

The restoration is described as the minimization of the functional

$$E(u) = \min_{u} \left[\frac{1}{2} \|I - Hu\|^2 + \lambda \int |\nabla u| dxdy \right], \qquad (8)$$

where I is the blurred observed image, H is the blurring operator (Eq. (7)), u is the unknown sharp image, and λ is a positive regularization constant, which we have set according to a fine-tuning procedure [18].

We performed several experiments to illustrate the appropriateness of the SV approach for restoring blurred retinal images. Moreover, to achieve an artifact free restoration we used our strategy for detecting the non-valid local PSFs and replacing them with a corrected one [26, 27, 29].

To demonstrate the capabilities of our method, we show the restoration results on *real cases* from the clinical practice. A typical source of retinal image degradation comes from patients with corneal defects in which the cornea has an irregular structure (Fig. 12). This induces optical aberrations, which are mainly responsible for the space-variant blur observed in the retinal image. In Fig. 13(a), a full color retinal image is shown, in which three small hemorrhages are more easily discernible in the restored image, along with

small blood vessels. Another retinal image, shown in Fig. 13(b), reveals a clear improvement in resolution with a much finer definition of blood vessels.

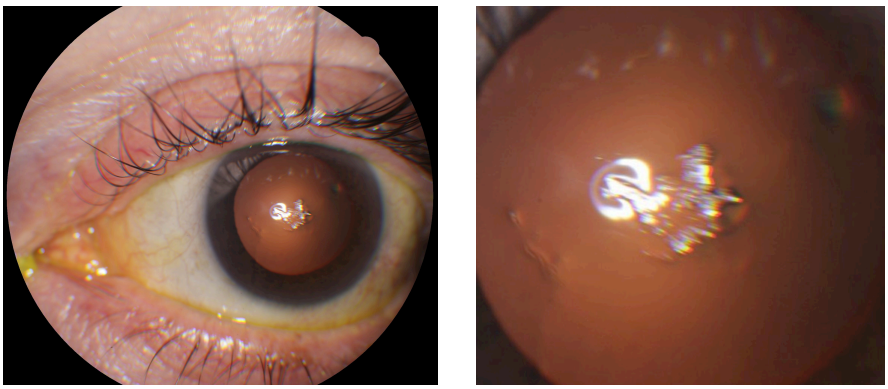

Fig. 12 (a) Left: Eye with corneal defects that induce retinal images with SV degradation. Right: zoomed region.

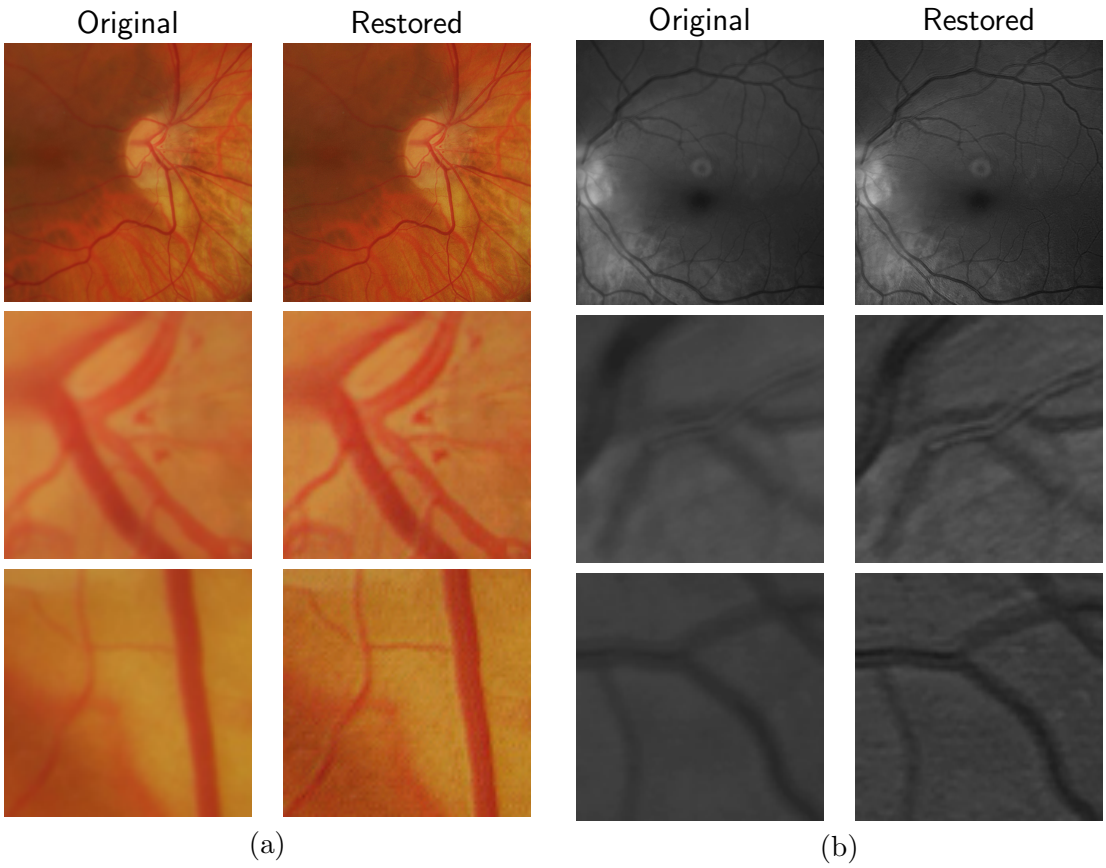

Fig. 13 Other retinal images restored with the proposed method. First row: original and restored full-size retinal images. Second and third rows: image details.

In addition, we processed retinal angiography images to test our method against a different imaging modality. The ophthalmologists use these photographs both for diagnosis and as a guide to patient treatment. Ocular angiography differs from fundus photography in that it requires an exciter--barrier filter set. The retinal angiography shown in Fig. 14 is degraded with a mild SV blur that hinders the resolution of small—yet important—details. The restoration serves to overcome this impediment; this can be observed from the zoomed-detail of the restored image.

5. Conclusions

As we have seen the application of digital image processing techniques for medical image analysis, in this case retinal images, is not only extremely beneficial but can also prove to be effective and cost-efficient for disease management, diagnosis, screening, etc. The increasing need for early detection and screening, along with the ever-increasing costs of health care, are likely to be the driving force for the rapid adoption and translation of research findings into clinical practice. Our contributions are a step toward that goal. However, there are many remaining obstacles and there is an implicit need to test and develop more robust techniques, to test many more patients, different illnesses, etc., before this technology is ready for everyday use. In our particular case, we need to further develop the PSF estimation and selection technique before we can have a fully automated fundus image enhancement algorithm. We believe that mobile computing devices will pave the way in the upcoming years for health-oriented applications with the intent of increasing global health-care access.

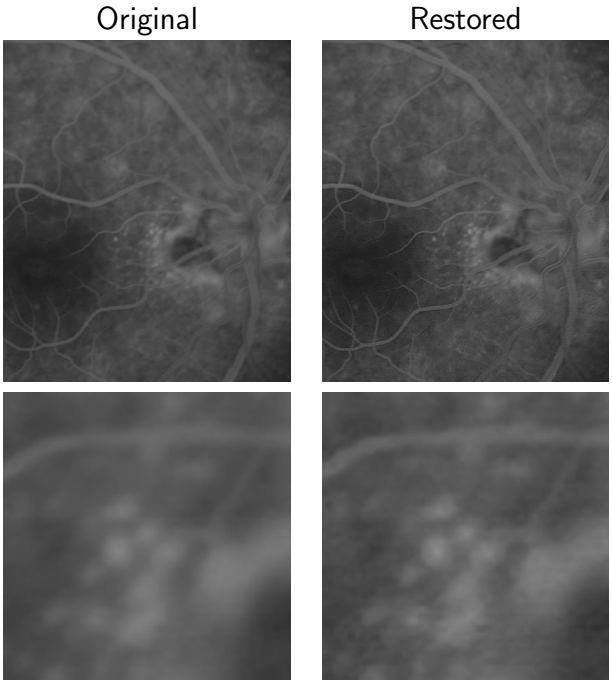

Fig. 14 Restoration of a retinal angiography. First row: original and restored full retinal images. Second row: image details.

Acknowledgements

This research has been partly funded by the Spanish Ministerio de Economía y Competitividad (project DPI2013-43220-R). The first author also thanks the Spanish Ministerio de Educación for an FPU doctoral Scholarship.

